

Systematic study of Optical Feshbach Resonances in an ideal gas

S. Blatt¹, T. L. Nicholson¹, B. J. Bloom¹, J. R. Williams¹, J. W. Thomsen¹*, P. S. Julienne², and J. Ye¹

¹JILA and Department of Physics, NIST and University of Colorado, Boulder, CO 80309-0440, USA

²Joint Quantum Institute, NIST and the University of Maryland, Gaithersburg, MD 20899-8423, USA.

(Dated: June 3, 2011)

Using a narrow intercombination line in alkaline earth atoms to mitigate large inelastic losses, we explore the Optical Feshbach Resonance (OFR) effect in an ultracold gas of bosonic ^{88}Sr . A systematic measurement of three resonances allows precise determinations of the OFR strength and scaling law, in agreement with coupled-channels theory. Resonant enhancement of the complex scattering length leads to thermalization mediated by elastic and inelastic collisions in an otherwise ideal gas. OFR could be used to control atomic interactions with high spatial and temporal resolution.

PACS numbers: 34.50.Rk, 34.50.Cx, 32.80.Qk

The ability to control the strength of atomic interactions has led to explosive progress in the field of quantum gases for studies of few- and many-body quantum systems. This capability is brought about by magnetic field-induced Feshbach scattering resonances (MFR) [1], where both the magnitude and sign of low-energy atomic interactions can be varied by coupling free particles to a molecular state. MFR in ultracold alkali atoms have been used to realize novel few-body quantum states and study strongly correlated many-body systems and phase transitions [1, 2]. However, magnetic tuning has limited current experiments to relatively slow time scales and low spatial resolution. Higher resolution could be achieved by controlling MFR optically [3].

Scattering resonances can also arise under the influence of laser light tuned near a photoassociation (PA) resonance [4] where free atom pairs are coupled to an excited molecular state [5, 6]. This Optical Feshbach Resonance (OFR) is expected to enable new and powerful control with high spatial and temporal resolution. OFR has been studied in thermal [7] and degenerate [8, 9] gases of Rb, but it was not found useful due to large photoassociative losses. Much narrower optical intercombination lines are available in alkaline earth atoms and are predicted to overcome this loss problem [10]. Independently, ultracold alkaline earth atoms have recently emerged to play leading roles for quantum metrology [11–13] where precision measurement and many-body quantum systems are combined to study new quantum phenomena [14, 15]. Degenerate gases of alkaline earth atoms have recently become available [16]. Due to the lack of magnetic structure in the ground state of these atoms, the OFR effect could become an important tool for controlling their interactions. OFR work on Yb [17, 18] has been limited to studying the induced change in scattering phase shifts and PA rates. Dominant PA losses are evident in all of the OFR experiments listed above. Light-induced elastic collisions for thermalization were not observed.

In this Letter, we study the OFR effect across multiple resonances in a metastable molecular potential of ^{88}Sr . The aim of this work is to test the practical appli-

cability of OFR for engineering atomic interactions in the presence of loss, similar to the successful application of a decaying MFR [19]. For ^{88}Sr , OFR is predicted [10] to allow changes in the scattering length by more than a factor of 100 with low losses by using large detunings ($\mathcal{O}(10^5)$ linewidths) from the least-bound vibrational level [20]. We tested this proposal and find experimentally that the existing isolated resonance model [6] only describes the experiment in the small detuning regime. Large detunings from a molecular resonance require a full coupled-channels description of the molecular response. Supported by this new theory framework, we present a systematic experimental study of the OFR-enhanced complex scattering lengths and demonstrate OFR-induced thermalization in an ultracold gas.

Bosonic ^{88}Sr has an s -wave background scattering length $a_{\text{bg}} = -1.4(6)a_0$ [21], where a_0 is the Bohr radius. The small $|a_{\text{bg}}|$ makes the sample effectively non-interacting and provides an ideal testing environment for OFR. Figure 1a shows the ground (${}^1\text{S}_0$ - ${}^1\text{S}_0$ 0_g) and lowest excited state (${}^1\text{S}_0$ - ${}^3\text{P}_1$ 0_u) molecular potentials of Sr_2 , which are coupled by a PA laser near the atomic transition at $\lambda_a = 689$ nm. The vibrational levels investigated are labelled by their quantum number n , counted as negative integers from the free particle threshold. For a given PA laser detuning from threshold, the Franck-Condon principle localizes the atom-light interaction in the vicinity of the Condon point [6].

When detuning the PA laser across a vibrational resonance, the s -wave scattering length shows a dispersive behavior, just as for a MFR. However, the finite lifetime of the excited molecular state leads to loss intrinsic to OFR. This process can be described [22] akin to decaying MFR [1, 19] with a complex s -wave scattering length $\alpha(k) \equiv a(k) - ib(k)$ that depends on the relative momentum $\hbar k$ and a PA line strength factor $\ell_{\text{opt}} = \frac{\lambda_a^3}{16\pi c} \frac{|\langle n|E \rangle|^2}{k} I$, called the optical length [10, 23]. Here, c is the speed of light, and ℓ_{opt} scales linearly with PA intensity I and free-bound Franck-Condon factor $|\langle n|E \rangle|^2$ per unit collision energy $E = \hbar^2 k^2 / (2\mu)$ at reduced mass $\mu = m_{\text{Sr}}/2$. In the isolated resonance approximation [6] the inelastic

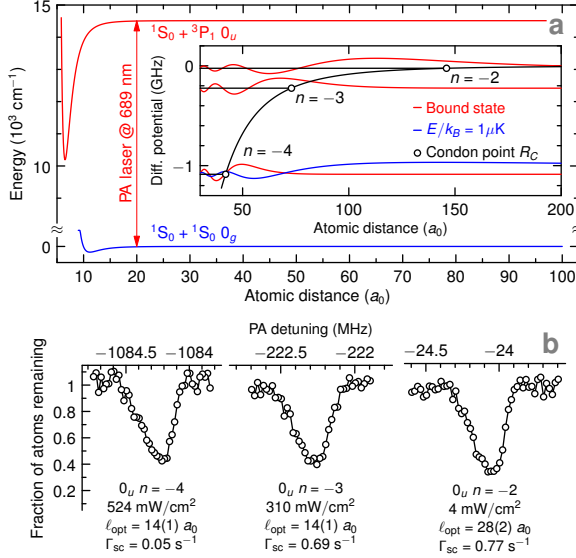


FIG. 1: (a) Ground (blue) and excited (red) molecular potentials of Sr_2 . The inset shows the difference potential after subtracting the optical frequency. Horizontal lines indicate bound molecular states n in the excited potential. The free particle (bound state) radial wave function is indicated in blue (red). (b) Loss spectra for 0_u $n = -2, -3$, and -4 for exposure time $\tau_{\text{PA}} = 200$ ms and comparable mean density. I is scaled to keep Γ_{sc} sufficiently small. The similarity of the spectra demonstrates the universal scaling with $\ell_{\text{opt}} \propto |\langle n | E \rangle|^2 I$.

collision rate is [22]

$$K_{\text{in}}(k) = \frac{4\pi\hbar}{\mu} \frac{\frac{\ell_{\text{opt}}\gamma_m}{\gamma}}{(\Delta + E/\hbar)^2/\gamma^2 + [1 + 2k\frac{\ell_{\text{opt}}\gamma_m}{\gamma}]^2/4}, \quad (1)$$

where Δ is the laser detuning from molecular resonance [22]. We have accounted for extra molecular losses with $\gamma > \gamma_m = 2\gamma_a$, where γ_m is the linewidth of the molecular transition and $\gamma_a = 2\pi \times 7.5$ kHz is the atomic linewidth. Neglecting a_{bg} for ⁸⁸Sr gives $K_{\text{el}}(k) \simeq 2k\frac{\ell_{\text{opt}}\gamma_m}{\gamma} K_{\text{in}}(k)$. The elastic-to-inelastic collision ratio $K_{\text{el}}/K_{\text{in}}$ becomes less favorable for smaller k .

We load $\sim 5 \times 10^4$ atoms from a magneto-optical trap operating on the ${}^1\text{S}_0$ - ${}^3\text{P}_1$ intercombination transition into a crossed optical dipole trap formed by tilted horizontal (H) and vertical (V) beams (1064 nm), with trap depths ~ 15 μK and ~ 7 μK , respectively. The trapped sample shows a clear kinetic energy inhomogeneity between the H and V axes (2-2.5 μK vs. 3-4 μK), due to the negligible a_{bg} , consistent with a thermal distribution energy-filtered by the trap potential. Typical in-trap cloud diameters are 45-55 μm . The PA beam intersects the trap with a waist of 41 μm [22].

A representative survey of PA resonances in the ${}^1\text{S}_0$ - ${}^3\text{P}_1$ 0_u potential is shown in Fig. 1b. The PA laser with intensity I , adjusted to achieve similar ℓ_{opt} for all spectra shown, interacts with the sample for τ_{PA} . Photon-atom

scattering at rate Γ_{sc} and subsequent radiation trapping set the maximum usable I for a given detuning from the atomic line [22]. In addition to the vibrational levels indicated in Fig. 1a, the $n = -1$ vibrational state exists at -0.4 MHz detuning from the threshold, which leads to a PA resonance with a very large line strength ℓ_{opt}/I [20]. The isolated resonance theory indicates that operating with a large I at $\mathcal{O}(10^5\gamma_a)$ detuning from the $n = -1$ state should allow modifications to $a(k)$ of $\mathcal{O}(100a_0)$ [10]. This prediction relied on extrapolating the large line strength of the $n = -1$ state across multiple intermediate PA resonances. However, with I up to 1 kW/cm² and detunings up to -1.5 GHz, we did not observe any effects due to elastic collisions.

The discrepancy between theory and experiment stimulated a coupled-channels treatment of an atomic collision in a radiation field that properly switches between the short range molecular states and two field-dressed separated atoms [22, 24, 25]. In the coupled-channels theory, the two coupled excited potentials (0_u , 1_u) have the form of Ref. [20], with an added imaginary term $-i\hbar\gamma_m/2$. The ground state potential uses the dispersion coefficients of Ref. [26], has a scattering length of $-1.4 a_0$, and reproduces the bound state data of Ref. [21] to better than 0.4%. Coupled-channels calculations do not assume isolated resonances, and all 0_u and 1_u molecular eigenstates emerge from the calculation as interfering, decaying scattering resonances [1].

Figures 2c and d show that the coupled-channels model reproduces the isolated resonance expressions [1, 6] for $\alpha(k)$ and the rate constants as long as Δ is small compared to the spacing between molecular levels. However, the coupled-channels K_{el} returns to its background value $K_{\text{el}}^{\text{bg}}$ in between resonances regardless of their relative strengths. The dotted line indicates $K_{\text{el}}^{\text{bg}}(a_{\text{bg}})$ at $E/k_B = 4$ μK in Fig. 2a (Fig. 2d). These calculations show that each molecular line behaves as an isolated resonance near its line center. For detunings comparable to the molecular level spacing, the isolated resonance expressions cannot be used.

At intermediate detunings, $|\Delta| \gg \gamma(1 + 2k\ell_{\text{opt}}\frac{\gamma_m}{\gamma})$, $\alpha(k)$ can be written in the standard form for MFR [22],

$$\lim_{k \rightarrow 0} \alpha(k) = a_{\text{bg}} \left(1 - \frac{w}{\Delta} + \frac{i}{2} \frac{w\gamma}{\Delta^2} \right), \quad (2)$$

where $w \equiv -\ell_{\text{opt}}\gamma_m/a_{\text{bg}}$. To obtain a meaningful change in scattering length, $\ell_{\text{opt}}\gamma_m/\Delta$ needs to be sufficiently large, and the imaginary part $b = \frac{1}{2}\ell_{\text{opt}}\gamma_m\gamma/\Delta^2$ needs to be sufficiently small. Since $K_{\text{in}} \simeq (2 \times 10^{-12} \text{ cm}^3/\text{s}) (b/a_0)$, for a density of $\rho = 10^{12} \text{ cm}^{-3}$ and $b = 0.1a_0$, $K_{\text{in}}\rho = \Gamma_{\text{sc}}$ for $I = 53 \text{ W/cm}^2$ assumed for Figs. 2c,d. Thus, the calculations predict that changes in the scattering length of order $10 a_0 \gg |a_{\text{bg}}|$ should be possible with $\mathcal{O}(100 \gamma_m)$ detunings on timescales of 200 ms.

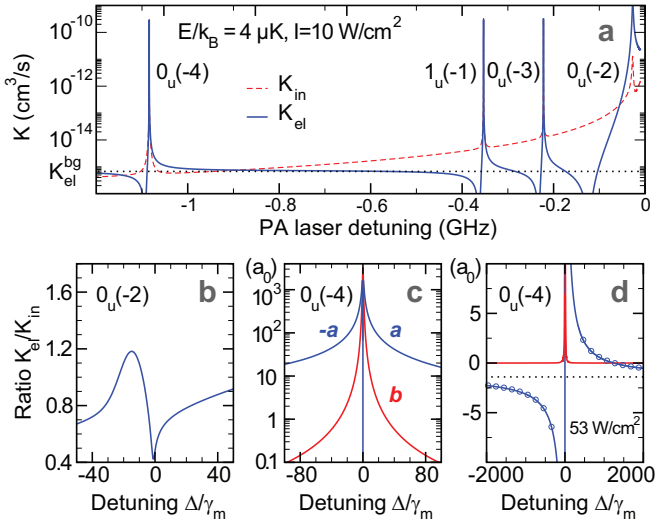


FIG. 2: (a) Coupled-channels calculations of K_{el} and K_{in} at $E/k_B = 4 \mu\text{K}$ and $I = 10 \text{ W/cm}^2$, versus PA laser detuning from atomic resonance. Each resonance peak is labeled by its electronic symmetry 0_u or 1_u and n . Between resonances, K_{in} is only approximate. (b) Ratio of thermally-averaged rate constants at $2 \mu\text{K}$ for Δ/γ_m near $0_u(-2)$. $I = 44 \text{ mW/cm}^2$ gives the same $\ell_{\text{opt}} = 360a_0$ as for the conditions in Fig. 4b. (c) Zero energy limit of $a(k)$ and $b(k)$ for detuning near the $0_u(-4)$ feature. (d) Same calculation as in (c) at large detuning. Here, the isolated resonance results (solid lines) agree with the coupled-channels theory (circles).

To investigate the utility of OFR, we systematically characterized three different resonances and determined their universal scaling. Because $K_{\text{el}}/K_{\text{in}} \propto k\ell_{\text{opt}}$, inelastic collisions dominate the dynamics of the sample for small $\ell_{\text{opt}} \ll (2\langle k \rangle)^{-1} = \frac{\hbar}{2}\sqrt{\pi/(8\mu k_B T)}$, where the angled brackets indicate a k -average at temperature T , and k_B is the Boltzmann constant. In this regime, the result of scanning the PA laser across resonance is a loss feature that shows no dependence on elastic collision processes.

A typical PA loss feature for small ℓ_{opt} is shown in Fig. 3a, where the final atom number after application of PA light is shown with respect to PA detuning from ${}^1\text{S}_0-{}^3\text{P}_1$. The per-axis kinetic energies [22] for this scan correspond to a horizontal (vertical) temperature $T_H(T_V) = 2 \mu\text{K}$ ($3 \mu\text{K}$), resulting in the typical thermal tail towards the red side of the resonance [27]. The solid line is a result of solving [28]

$$\dot{\rho}(\mathbf{x}, t) = -2\bar{K}_{\text{in}}(\mathbf{x}) \frac{\rho^2(\mathbf{x}, t)}{2} - \frac{\rho(\mathbf{x}, t)}{\tau_{\text{bg}}}, \quad (3)$$

with single particle density ρ , thermally-averaged inelastic collision rate $\bar{K}_{\text{in}}(\mathbf{x}) \equiv \langle K_{\text{in}}(k, \Delta, \mathbf{x}) \rangle$ [22], and vacuum-limited trap lifetime $\tau_{\text{bg}} \simeq 1.3 \text{ s}$. Equation 3 is solved at each \mathbf{x} and we integrate the density to obtain the number of atoms at the end of the PA pulse. We then use Eq. 3 to fit to the experimental data [22] and extract ℓ_{opt} and the position of the line center. Figure 3b

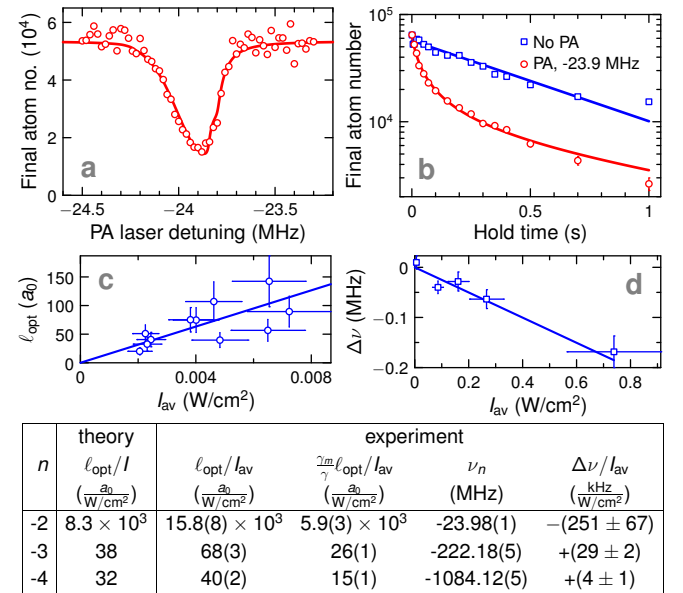


FIG. 3: (a) Typical PA loss feature for $n=-2$ in the low intensity regime at $I_{\text{av}} = 7 \text{ mW/cm}^2$, with density-profile-averaged PA intensity I_{av} [22]. (b) Time evolution of the trapped sample with (circles) and without PA light (squares). The two-body loss curve with PA is fit with a thermally averaged model (solid curve). (c) Linear increase of ℓ_{opt} with I_{av} for $\ell_{\text{opt}} \ll 1/(2\langle k \rangle)$. (d) Molecular line center shift $\Delta\nu$ for large I_{av} and decreased τ_{PA} . For each n , OFR parameters from the coupled-channels calculation and the experiment are summarized in the table at the bottom. Here, ν_n is the zero-intensity molecular line center with respect to ${}^1\text{S}_0-{}^3\text{P}_1$, and $\Delta\nu/I_{\text{av}}$ characterizes the molecular ac Stark shift [23].

shows the time dependence of the same photoassociative loss process. Two-body loss is evident under resonant PA light.

From the experimental data we extract two independent quantities: $\ell_{\text{opt}}\gamma_m$ and an increased molecular loss rate $\gamma \simeq 2.7\gamma_m$. We have ruled out magnetic field or PA laser noise as a source of broadening. Instead, we conclude that this extra broadening is related to a faster molecular decay rate, which is consistent with our earlier measurements [20] and Rb results [8].

The measurements were performed for a range of ℓ_{opt} by adjusting I_{av} . Multiple molecular resonances were measured and results for $n=-2$ are shown in Fig. 3c. The optical length data is fit with a linear function and the results are summarized in the table at the bottom. The fit coefficient $\ell_{\text{opt}}/I_{\text{av}}$ is given by the free-bound Franck-Condon factor and decreases drastically with decreasing n . Figure 3d exemplifies similar measurements done to determine the line shift $\Delta\nu$ with I_{av} . Linear shift coefficients $\Delta\nu/I_{\text{av}}$ and zero intensity line positions ν_n with respect to the atomic transition are also shown in the table. The sign and magnitude of $\Delta\nu/I_{\text{av}}$ are consistent with the predictions in Ref. [23].

At larger optical lengths ($\ell_{\text{opt}}\gamma_m/\gamma \sim 100a_0$), elastic

collisions start to influence the dynamics of the system. We show the atom loss with respect to PA laser detuning for $n=-2$ in Fig. 4a. Both in-trap size and kinetic energy are measured by absorption imaging [22]. Far detuned from the resonance, the gas is almost ideal, as shown by the persistent kinetic energy inhomogeneity along H and V in Fig. 4b. On resonance (vertical dashed line), inelastic collisions dominate and cause heating. For red detuning from the molecular resonance, the temperatures approach each other by cross-thermalization [29].

The measured cloud widths w_H and w_V confirm that the potential energy follows the kinetic energy (Fig. 4c) since particles oscillate in the trap many times between collisions. Similar measurements were performed for $n=-3$ and $n=-4$, and we find that the same dispersive behavior in temperatures and widths appears around $2\langle k \rangle \ell_{\text{opt}} \gamma_m / \gamma \sim 30\%$ at $\tau_{\text{PA}} = 200$ ms. The data can be understood by a simple picture of competition between K_{el} and K_{in} , which average differently with k in a thermal sample [see Eq. (1)], and thus peak at different values of Δ . Elastic collisions cause cross-dimensional thermalization and tend to equalize T_H and T_V . Since inelastic collisions predominantly remove cold atoms from the densest part of the cloud, the resulting loss increases the average system energy via anti-evaporation.

This behavior is confirmed by a Monte-Carlo simulation, where 55×10^3 particles are simulated and each particle undergoes elastic and inelastic collisions with an initial phase-space distribution matched to the experimental conditions [22]. The solid lines overlaid on the experimental data in Fig. 4 are the simulation results. An average ratio of elastic to inelastic collisions per particle from the simulation is shown in Fig. 4d. The dispersive shapes are also predicted by the coupled-channels model (see Fig. 2b) and their shape is sensitive to γ . Combined with the low ℓ_{opt} data in Fig. 3, the entire simulation reproduces the experimental data only when $\gamma = 2\pi \times 40(5)$ kHz without other free parameters.

We conclude that the isolated resonance approximation universally describes OFR in the vicinity of each resonance. The coupled-channels calculation includes all interference effects between resonances, and differs from the isolated resonance approximation at large detuning between resonances. Our experiment contradicts previous predictions based on extrapolations of an isolated resonance to large detunings [10, 20]. We have validated the linear line strength scaling and linear resonance shift with I and have observed a clear modification of both $a(k)$ and $b(k)$. For the values of $\ell_{\text{opt}} \gamma_m / \gamma$ achieved here, inelastic losses still contribute significantly and $\langle K_{\text{el}} / K_{\text{in}} \rangle$ becomes even less favorable with decreasing T . However, the OFR effect can modify interactions in a degenerate gas of alkaline earth atoms and the desired change of $a(k)$ is achieved at the smallest Δ / γ constrained by both molecular and atomic loss processes over a given experimental timescale [22].

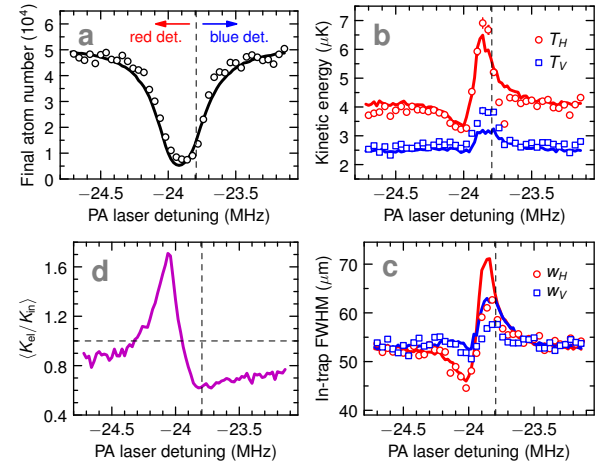


FIG. 4: Elastic contribution to the scattering cross section for $n=-2$ at $I_{\text{av}} = 22$ mW/cm² (open circles) and results of a Monte-Carlo simulation (solid lines) using Eq. 1 in a crossed dipole trap for $\ell_{\text{opt}} \gamma_m / \gamma = 140a_0$. (a) Atom loss as a function of PA laser detuning from the atomic $^1\text{S}_0$ - $^3\text{P}_1$ resonance. In panels b and c, blue (red) data points and solid lines indicate the corresponding quantities for the vertical (horizontal) trap axis. (b) Change in kinetic energy derived from time-of-flight images, and (c) potential energy change corresponding to varying in-trap density profile. (d) The resultant ratio of elastic and inelastic collisions per particle, averaged over τ_{PA} .

We thank C. Greene, P. Zoller, and G. Campbell for discussions and contributions. J. R. W. is an NRC Fellow. Our work is funded by DARPA OLE, NIST, & NSF.

-
- * Permanent address: The Niels Bohr Institute, Universitetsparken 5, 2100 Copenhagen, Denmark.
- [1] C. Chin *et al.*, Rev. Mod. Phys. **82**, 1225 (2010).
 - [2] I. Bloch, J. Dalibard, and W. Zwerger, Rev. Mod. Phys. **80**, 885 (2008); S. Giorgini, L. P. Pitaevskii, and S. Stringari, *ibid.*, 1215; W. Ketterle and M. W. Zwierlein, in *Ultracold Fermi Gases, "Enrico Fermi" Course CLXIV* (2008), p. 95.
 - [3] D. M. Bauer *et al.*, Nature Physics **5**, 339 (2009).
 - [4] K. Jones *et al.*, Rev. Mod. Phys. **78**, 483 (2006).
 - [5] P. Fedichev *et al.*, Phys. Rev. Lett. **77**, 2913 (1996).
 - [6] J. Bohn and P. Julienne, Phys. Rev. A **60**, 414 (1999).
 - [7] F. Fatemi, K. Jones, and P. Lett, Phys. Rev. Lett. **85**, 4462 (2000).
 - [8] M. Theis *et al.*, Phys. Rev. Lett. **93**, 123001 (2004).
 - [9] G. Thalhammer *et al.*, Phys. Rev. A **71**, 033403 (2005).
 - [10] R. Ciurylo, E. Tiesinga, and P. S. Julienne, Phys. Rev. A **71**, 030701 (2005).
 - [11] T. Akatsuka, M. Takamoto, and H. Katori, Nature Physics **4**, 954 (2008).
 - [12] G. K. Campbell *et al.*, Science **324**, 360 (2009).
 - [13] N. Poli *et al.*, Phys. Rev. Lett. **106**, 038501 (2011).
 - [14] M. D. Swallows *et al.*, Science **331**, 1043 (2011).
 - [15] A. V. Gorshkov *et al.*, Nature Physics **6**, 289 (2010).
 - [16] Y. Takasu *et al.*, Phys. Rev. Lett. **91**, 040404 (2003);

- S. Kraft *et al.*, Phys. Rev. Lett. **103**, 130401 (2009); S. Stellmer *et al.*, *ibid.*, 200401; Y. de Escobar *et al.*, *ibid.*, 200402.
- [17] K. Enomoto *et al.*, Phys. Rev. Lett. **101**, 203201 (2008).
- [18] R. Yamazaki *et al.*, Phys. Rev. Lett. **105**, 050405 (2010).
- [19] D. Naik *et al.*, Euro. Phys. J. D online, doi:10.1140/epjd/e2010-10591-2 (2011).
- [20] T. Zelevinsky *et al.*, Phys. Rev. Lett. **96**, 203201 (2006).
- [21] Y. de Escobar *et al.*, Phys. Rev. A **78**, 062708 (2008).
- [22] See accompanying supplementary material for details.
- [23] R. Ciuryło, E. Tiesinga, and P. S. Julienne, Phys. Rev. A **74**, 022710 (2006).
- [24] P. Julienne and F. Mies, Phys. Rev. A **34**, 3792 (1986).
- [25] R. Napolitano, J. Weiner, and P. S. Julienne, Phys. Rev. A **55**, 1191 (1997).
- [26] S. G. Porsev and A. Derevianko, J. Exp. Theor. Phys. **102**, 195 (2006).
- [27] R. Ciuryło *et al.*, Phys. Rev. A **70**, 062710 (2004).
- [28] J. P. Burke, Jr., Ph.D. thesis, Univ. of Colorado (1999).
- [29] J. Goldwin *et al.*, Phys. Rev. A **71**, 043408 (2005).

SUPPLEMENTARY MATERIAL

Scattering matrix, cross sections, and collision rates

The collision of two identical bosons in the low energy near-threshold limit can be described in a scattering matrix treatment by a single *s*-wave scattering matrix element, $S(k) = e^{2i\eta(k)}$, where $\hbar k$ is the relative momentum of the collision pair and $\eta(k)$ is the scattering phase shift due to interactions. When there is loss of scattering flux from the entrance channel, as is the case of a decaying optical Feshbach resonance, it is convenient to define a complex energy-dependent scattering length $\alpha(k)$, related to the complex phase $\eta(k)$ and *S*-matrix element by [1, 2]

$$\alpha(k) \equiv a(k) - ib(k) \equiv -\frac{\tan \eta(k)}{k} = \frac{1}{ik} \frac{1 - S(k)}{1 + S(k)}. \quad (4)$$

This reduces to the usual definition of complex scattering length as $k \rightarrow 0$. The respective elastic and inelastic *s*-wave collision cross sections are [2, 3]

$$\begin{aligned} \sigma_{\text{el}}(k) &= \frac{2\pi}{k^2} |1 - S(k)|^2 = 8\pi |\alpha(k)|^2 f^2(k), \\ \sigma_{\text{in}}(k) &= \frac{2\pi}{k^2} (1 - |S(k)|^2) = \frac{8\pi}{k} b(k) f(k), \end{aligned} \quad (5)$$

where $f(k) = [1 + k^2 |\alpha(k)|^2 + 2kb(k)]^{-1} \rightarrow 1$ as $k \rightarrow 0$ and μ is the reduced mass of the pair. The second relations in Eq. 5 follow from the definition in Eq. 4. The corresponding collision rate coefficients are

$$\begin{aligned} K_{\text{el}}(k) &= \frac{\hbar k}{\mu} \sigma_{\text{el}}(k), \\ K_{\text{in}}(k) &= \frac{\hbar k}{\mu} \sigma_{\text{in}}(k). \end{aligned} \quad (6)$$

When the entrance channel is coupled by a single frequency laser to a single excited molecular bound state of the pair, the isolated resonance approximation for the field-dressed *s*-wave scattering matrix element can be written as [4, 5],

$$S(k) \simeq e^{2i\eta_{\text{bg}}(k)} \left(1 - i \frac{\Gamma_s(k)}{E/\hbar + \Delta + i(\gamma + \Gamma_s(k))/2} \right). \quad (7)$$

Here $E = \hbar^2 k^2 / 2\mu$ is the collision energy with $\mu = m_{\text{Sr}}/2$. The laser detuning Δ from the PA resonance includes the light shift [5] to simplify the presentation (see Eq. 20 for a full expression).

The stimulated width $\Gamma_s(k) \equiv 2k\ell_{\text{opt}}(k)\gamma_m$ is the induced coupling between the free particle state $|E\rangle$ and the excited molecular state $|n\rangle$. Here $\gamma_m = 2\gamma_a$ is the linewidth of the molecular transition and $\gamma_a = 2\pi \times 7.5$ kHz is the atomic linewidth. We have allowed for extra molecular losses by letting $\gamma > \gamma_m$. The optical length

$$\ell_{\text{opt}} = \frac{\lambda_a^3}{16\pi c} \frac{|\langle n|E \rangle|^2}{k} I, \quad (8)$$

where c is the speed of light, is a PA resonance-dependent line strength parameter [5, 7]. Under the Wigner threshold law, the free-bound Franck-Condon factor per unit collision energy $|\langle n|E \rangle|^2 \propto k$, and we checked numerically that it is a very good approximation to take ℓ_{opt} to be independent of collision energy for temperatures $< 10 \mu\text{K}$. The optical length is also independent of the atomic oscillator strength, and it scales linearly with PA intensity I .

Combining Eq. 7 with Eqs. 4-6 gives the near-threshold isolated resonance approximation to the OFR inelastic loss rate coefficient:

$$K_{\text{in}}(k) = \frac{4\pi\hbar}{\mu} \frac{\frac{\ell_{\text{opt}}\gamma_m}{\gamma}}{(\Delta + E/\hbar)^2/\gamma^2 + [1 + 2k\frac{\ell_{\text{opt}}\gamma_m}{\gamma}]^2/4}. \quad (9)$$

The background *s*-wave scattering length a_{bg} is defined in the absence of a resonance as

$$a_{\text{bg}} = -\lim_{k \rightarrow 0} \frac{\tan \eta_{\text{bg}}(k)}{k}. \quad (10)$$

If we neglect a_{bg} for ^{88}Sr , we find a simple expression for the OFR-induced elastic collision rate coefficient for an ideal ultracold gas

$$K_{\text{el}}(k) \simeq 2k \frac{\ell_{\text{opt}}\gamma_m}{\gamma} K_{\text{in}}(k). \quad (11)$$

Power broadening is included via $\Gamma_s(k)$ in the denominator of Eq. 7, which corresponds to $2k\frac{\ell_{\text{opt}}\gamma_m}{\gamma}$ in the denominator of Eq. 9. From the expressions for elastic and inelastic collision rates, we see that the relevant strength parameter in the presence of extra molecular

loss is the rescaled optical length $\ell_{\text{opt}} \frac{\gamma_m}{\gamma}$. Elastic collisions and power broadening only become important for the dynamics when

$$2k \frac{\ell_{\text{opt}} \gamma_m}{\gamma} \sim 1. \quad (12)$$

Coupled Channels Calculations

The simplest way to do a calculation of the elastic and inelastic collision properties of an optical Feshbach resonance is to set up a coupled channels model for the collision of field-dressed states in a laser field of fixed frequency [4, 6]. We use the simplest three-channel model that is sufficiently complete to represent nonperturbatively the optically induced $S(k)$ for an interfering spectrum of excited state resonances. One channel represents the ground state with potential $V_g(R)$ and two channels represent the two excited states 0_u and 1_u that correlate with the separated atom limit $^1S_0 + ^3P_1$ with respective complex potentials V_{0u} and V_{1u} . These potentials are shifted to include the asymptotic detuning of the laser frequency from atomic resonance. It is necessary to include both 0_u and 1_u excited states to correctly calculate the complex scattering length near an isolated resonance of either state. This is because the molecular $J = 1$ excited states (J = total angular momentum quantum number) must become a mixture of s and d -waves at long range to properly go to separated atoms with 3P_1 quantized in a space frame instead of a molecular body frame [6]; otherwise, spurious $1/R^3$ resonant dipole terms would get mixed into the ground state potential and give invalid threshold scattering lengths.

The coupled channel potential matrix $\mathbf{V}(R)$ is found using the asymptotic representation of the two excited $J = 1$ molecular channels in terms of a pair of excited state s - and d -waves for the e parity block in Table 1 of Reference [6]:

$$\mathbf{V} = \begin{pmatrix} V_g & V_{\text{opt}} & 0 \\ V_{\text{opt}} & \frac{1}{3}(V_{0u} + 2V_{1u}) & \frac{\sqrt{2}}{3}(V_{1u} - V_{0u}) \\ 0 & \frac{\sqrt{2}}{3}(V_{1u} - V_{0u}) & \frac{1}{3}(2V_{0u} + V_{1u} + 6B) \end{pmatrix}, \quad (13)$$

where $6B = 6\hbar^2/(2\mu R^2)$ is the d -wave centrifugal energy. Here the row labels, in order from top to bottom, represent the $|j\ell JM\rangle = |0000\rangle$ ground state and $|1010\rangle$ and $|1210\rangle$ excited state channels of Ref. [6], where j is the atomic angular momentum for the collision partner to the 1S_0 atom, ℓ is partial wave, and JM represent the total angular momentum and its projection for the pair of interacting atoms. Since the excited bound states are relatively short range, we use the nonretarded optical coupling $V_{\text{opt}} = (2\pi I/c)^{1/2}d_m$, where $d_m = \sqrt{2}d_A$ and the atomic transition dipole $d_A = 0.086816$ atomic units corresponds to an atomic lifetime of $21.46 \mu\text{s}$. A

complete theory would use the retarded optical coupling. The zero of energy for ground state collisions is taken to be the lowest eigenvalue of this matrix to account for the energy shift of the field dressed molecule. The numerical S -matrix is calculated using standard coupled channels methods to calculate the wave function for the coupling matrix in Eq. 13.

While Reference [4] simulates the spontaneous radiative decay of the excited state by introducing artificial channels, here we include a complex term $-i\hbar\gamma/2$ in each of these excited state potentials to simulate this decay, where in our numerical calculations we take $\gamma = \gamma_m$. This leads to a non-unitary ground state S -matrix element such that $0 \leq 1 - |S(k)|^2 \leq 1$ gives probability of atom loss during a collision. In order to avoid problems with spurious asymptotic decay of the field dressed states, a tapered cutoff function is introduced so that decay is only turned on inside some characteristic distance, which we take to be $500 a_0$. We have verified that $a(k)$ is independent of this choice over the full range of detunings, even between resonances, and $b(k)$ is independent of this choice out to many linewidths away from an isolated resonance. However, in the far wings of a resonance between isolated resonances, $b(k)$ will depend on this choice, although molecular loss tends to be small in these regions. This dependence on cutoff is because our non-unitary theory does not distinguish between atomic and molecular light scattering when the atoms are far apart; the cutoff selects which distance inside of which an excitation is considered to be a molecular loss process instead of an atomic one. Thus the cutoff is taken to be on the order of but larger than the outer turning point of the excited molecular bound states.

Finally, we ignore coupling of the excited $J = 1$ molecular levels back to d -waves in the ground state. This means that our model only gets the s -wave but not the d -wave contributions to the excited state light shifts [5]. It would be straightforward to add an extra ground state channel to the numerical calculation to account for this.

While there are a number of ways our simple model can be improved, it gives a practical way to calculate the needed complex scattering length for characterizing the intercombination line OFR spectrum of alkaline earth atoms. The model gives two key results. First, it should correctly describe the variation of the real part of the scattering length as laser frequency is tuned across multiple resonances. Second, the isolated resonance approximation should correctly describe the molecular loss rate out to order of hundreds of line widths away from individual isolated resonances.

Experimental Setup

Details of the experimental setup can be found in Ref. [8]. Atoms are loaded into an optical dipole trap

from a magneto-optical trap operating on the $^1\text{S}_0$ - $^3\text{P}_1$ intercombination transition. A horizontal (H) and a vertical (V) beam intercept in the \hat{x} - \hat{z} plane to form a crossed dipole trap at the origin shown in Fig. 5 (drawing is to scale). Both beams are derived from the same 1064 nm laser and are linearly polarized along the \hat{y} axis with $1/e^2$ waists 63 μm and 53 μm , respectively. The optical beams point in the directions

$$\begin{aligned}\hat{k}_H &= -\cos\theta_H \hat{x} - \sin\theta_H \hat{z}, \\ \hat{k}_V &= -\cos\theta_V \hat{z} + \sin\theta_V \hat{x}, \\ \hat{k}_{\text{PA}} &= -\cos\theta_{\text{PA}} \hat{x} + \sin\theta_{\text{PA}} \hat{y},\end{aligned}\quad (14)$$

with $\theta_H = 16.0^\circ$, $\theta_V = 14.4^\circ$, and $\theta_{\text{PA}} = \pi/8$. The beams are linearly polarized along $\hat{\epsilon}_H = \hat{\epsilon}_V = \hat{y}$ and $\hat{\epsilon}_{\text{PA}} = \hat{z}$. The image plane is spanned by $\cos\frac{\pi}{8}\hat{x} - \sin\frac{\pi}{8}\hat{y}$ and \hat{z} . A bias magnetic field of $B_z \simeq 100$ mGauss defines the atomic quantization axis.

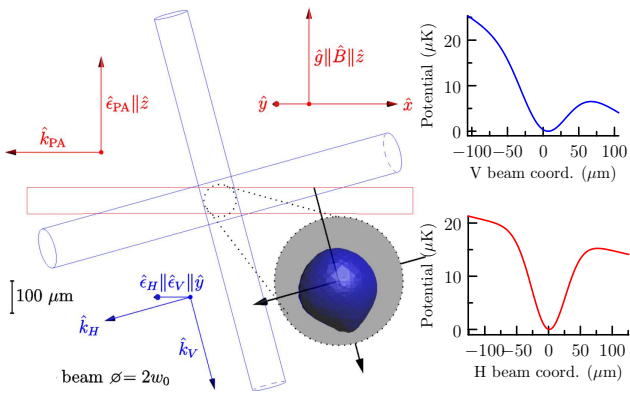


FIG. 5: Geometry of the experiment in the absorption image plane. The directions \hat{x} , \hat{y} , and \hat{z} define the lab frame, where both gravity \hat{g} and bias magnetic field \hat{B} are parallel to \hat{z} . Symbols \hat{k} are beam directions, and $\hat{\epsilon}$ are beam polarization vectors, where subscripts H , V , and PA indicate horizontal, vertical, and PA beams. H and V Gaussian beam profiles are shown in blue outline, PA Gaussian beam profile in red outline.

The focal condition is not critical to model the potential sufficiently well because of the large Rayleigh ranges (> 8 mm), and the Gaussian beam isosurfaces at the beam waist are almost cylindrical (blue outlines). Thus, the dipole trap potential due to each beam is modeled as

$$U_i(\mathbf{x}) \equiv -U_T^i \exp \left\{ -\frac{2}{w_i^2} \left([\hat{\epsilon}_i \cdot \mathbf{x}]^2 + [(\hat{k}_i \times \hat{\epsilon}_i) \cdot \mathbf{x}]^2 \right) \right\}, \quad (15)$$

with individual Gaussian beam trap depth [9]

$$U_T^i = \frac{P_i}{\pi c \epsilon_0 w_i^2} \text{Re } \alpha_{1\text{S}_0}(1064 \text{ nm}), \quad (16)$$

and total laser power P_i . The real part of the dynamic $^1\text{S}_0$ polarizability at 1064 nm is $\text{Re } \alpha_{1\text{S}_0}(1064 \text{ nm}) \simeq 239$ a.u. [10], with atomic unit of polarizability $4\pi\epsilon_0 a_0^3$.

The full model potential includes the gravitational acceleration g pointing along $-\hat{z}$ and is given by

$$U(\mathbf{x}) = U_H(\mathbf{x}) + U_V(\mathbf{x}) + m_{\text{Sr}} g z. \quad (17)$$

Gravity sets the trap depths of ~ 7 μK and ~ 15 μK along V and H . The two graphs on the right hand side of Fig. 5 show cuts through the model potential, which has been adjusted to match the measured trapping frequencies. An isosurface (dark blue) of the model potential at 7 μK is shown in the zoomed-out portion.

Typical kinetic energies are 2-4 μK , and in-trap Full Widths at Half Maximum (FWHM) are 45-55 μm . The PA beam (red outline) propagates along the horizontal image axis in the \hat{x} - \hat{y} plane with a waist $w_{\text{PA}} = 41$ μm and is linearly polarized along \hat{z} . Although the PA beam diameter $2\sqrt{2 \ln 2} \times w_{\text{PA}} \simeq 97$ μm is larger than the typical cloud FWHM, we use a density-averaged intensity $I_{\text{av}} = \int d^3x \rho(\mathbf{x}) I(\mathbf{x}) / \int d^3x \rho(\mathbf{x})$ to characterize the PA intensity interacting with the atoms. Typical values are $I_{\text{av}} \simeq (0.6 - 0.7) \times I_{\text{pk}}$, where $I_{\text{pk}} = \frac{2P}{\pi w_{\text{PA}}^2}$ is the Gaussian beam peak intensity for total beam power P .

In addition to scattering from the atomic transition with rate Γ_{sc} , the PA beam also adds to the optical trap slightly. For large intensities and small w_{PA} and especially in a standing wave configuration, this effect can become important. In this work, the additional trap depth introduced by the PA beam is typically < 0.1 μK .

Imaging Procedure and Analysis

We use a two-component long-working-distance microscope with 3 μm resolution at 532 nm. The imaging lens is placed outside the vacuum chamber at a distance of 150 mm from the atomic cloud. The second part of the telescope is an eyepiece mounted to a CCD camera with 1024×1024 square pixels of 13 μm width. The eyepiece includes an interference filter at 461 nm (intensity transmission 0.45 within 10 nm bandwidth, ND 5.0 otherwise). Time of flight measurements were used to determine an imaging magnification of 6.5, corresponding to 2.0 μm per pixel. We tested the imaging system resolution in a separate test setup that included the effect of an anti-reflection (AR) coated vacuum viewport, same as the one used on our vacuum chamber. Using incoherent white light filtered by the blue interference filter with transmissive test targets, resolutions of ~ 4 μm were measured. Absorption imaging with coherent light causes etaloning between the CCD chip and the glass plate that covers it. To reduce fringing, the glass plate surface is wedged at $\sim 1^\circ$ and AR coated for the imaging wavelength.

Without the elastic contribution of the OFR effect, the ^{88}Sr sample does not thermalize on experimental timescales due to its small a_{bg} , and it is important to obtain information about both the potential and kinetic

energies of the gas. We interleave experimental runs between in-situ imaging of the sample and imaging after the atoms were dropped for 1.5 ms by switching off the optical dipole trap. The first image gives information about the spatial density of the atomic cloud, and the second image measures the kinetic energy by time-of-flight expansion. We typically repeat this interleaved sequence 3-5 times and average the resulting in-situ and time-of-flight absorption images before performing data analysis. We also calculate the pixel-by-pixel studentized standard deviations which are used as weights in fitting the mean image and also enter the fit parameter error estimates. Both the mean and standard-deviation images are then rotated (with bilinear interpolation) by 14° about the center of the atom cloud to transform the images into the eigenframe of the trap. The pictures are then integrated along the horizontal (vertical) axis and are fit to extract w_H (w_V) with one-dimensional Gaussian distributions including a background offset and linear slope to account for residual fringing and CCD readout noise in the absorption image.

A common problem in imaging atomic clouds with large optical depth is light that does not interact with atoms hitting the camera in the same position. Common causes are forward scattering of photons into the imaging path or mixed probe polarization. Probing the 1S_0 - 1P_1 transition is insensitive to probe polarization even under a small bias magnetic field. To identify the possibility of a limiting optical depth $OD_{ceiling}$, a series of images were taken with increasing atomic density. We compared the peak optical depth in-situ versus the pixel-summed optical depth either of an in-situ or a corresponding time-of-flight image, and we estimate a conservative limit $OD_{ceiling} \geq 3.5$. Typical in-situ optical depths in this paper were below 2, so that we can neglect the effect.

For probe intensities larger than $0.1I_{sat}$, with saturation intensity $I_{sat} \simeq 40$ mW/cm², saturation of the imaging transition becomes important. To account for the saturated absorption, we correct the full expression for the OD to the linear Beer-Lambert regime [8, 11]. For each picture the saturation correction is applied on a pixel-by-pixel basis.

While the shadow image is forming and the atoms are scattering light, their momentum undergoes a random walk due to the spontaneous emission of blue photons. By examining the shadow image versus a reference image without atoms, we extract the number of photons that the atoms removed from the probe pulse. By varying the probe time, we find the cloud expansion as a function of the number of photons scattered and apply a corresponding correction to the cloud widths from both in-situ images and TOF images [8].

We extract the integrated OD of the mean image to obtain the atom number. Corrections for probe heating are then applied to the fitted widths. The in-situ image

widths are used to calculate the mean atomic density. Finally, we calculate a time-of-flight temperature corrected for finite size effects by the in-situ widths.

Loss Spectra ($2k\ell_{opt}\gamma_m/\gamma \ll 1$)

To extract $\ell_{opt}\gamma_m$ from the loss spectra, data was fit to an approximate expression for the integral of the atomic density, where the density after the PA pulse was calculated via the differential equation $\dot{\rho} = -\bar{K}_{in}\rho^2 - \rho/\tau_{bg}$ [12]. The initial density distribution was modelled as Gaussian with w_H and w_V . The width into the plane of the images was extrapolated from a Monte-Carlo simulation of the trap model potential. The fitting function is

$$N = \frac{2}{\sqrt{\pi}} \int_0^\infty du \frac{\sqrt{u} e^{-u}}{1 + \bar{K}_{in}(\Delta, u, \ell_{opt}\gamma_m, T) \tau_{eff} \rho_0 e^{-u}}, \quad (18)$$

with normalized dimensionless trap length scale u . This expression describes the number signal normalized to the measured atom number after the PA pulse of duration τ_{PA} and when the detuning from molecular resonance is large. The quantity $\tau_{eff} = \tau_{bg} e^{\tau_{hold}/\tau_{bg}} (e^{\tau_{PA}/\tau_{bg}} - 1)$ accounts for the fact that atoms are lost to one-body decay during the PA pulse with lifetime τ_{bg} and that we hold the atoms for $\tau_{hold} = 100$ ms between the end of the PA pulse and the imaging. The number ρ_0 is the peak density after the PA pulse and at large detuning. The definition of all other symbols follows the main text. To make the fit numerically tractable, the integral was approximated as a ten-term sum using Gauss-Laguerre quadrature.

The thermally-averaged inelastic collision rate per particle \bar{K}_{in} was derived from the s -wave scattering matrix of Bohn and Julienne, using the definition of the optical length $\ell_{opt} = \Gamma_s/2k\gamma_m$ in terms of the stimulated width Γ_s [4, 7]. Here, we use a thermally-averaged inelastic rate coefficient $\bar{K}_{in} \equiv \langle \hbar k \sigma_{in} / \mu \rangle$, where $\sigma_{in} = 2\frac{\pi}{k^2}(1 - |S|^2)$ [2]. The angular brackets denote a thermal average over the initial collision momenta. This average was performed on the inelastic rate coefficient (rather than the density after the PA pulse) under the assumption that prior to the PA pulse, many single-particle velocities exist in every differential volume in the trap. Since single collisions take place in a small volume, the spatial dependence of \bar{K}_{in} was carried through into the differential equation for the density rather than averaged out.

To fit the inelastic loss spectra, \bar{K}_{in} was expressed as

$$\begin{aligned} \bar{K}_{in}(\Delta, u, \ell_{opt}\gamma_m, T) &= \frac{8\sqrt{\pi}\hbar\ell_{opt}\gamma_m}{\mu} \int_0^\infty d\eta \frac{\gamma\sqrt{\eta} e^{-\eta}}{D^2 + \Gamma^2/4}, \\ D &\equiv \Delta + \frac{k_B T}{h}\eta - \nu_{rec} - \nu_s e^{-u/u_0}, \\ \Gamma &\equiv \gamma + 2k_{th}\ell_{opt}\gamma_m\sqrt{\eta}, \end{aligned} \quad (19)$$

with dimensionless relative momentum magnitude $\eta \equiv k^2/k_{\text{th}}^2$, thermal momentum $\hbar k_{\text{th}} = \sqrt{2\mu k_B T}$, center-of-mass PA photon recoil energy $\hbar\nu_{\text{rec}}$, trapping laser ac Stark shift at the center of the trap ν_s , and Planck's constant $\hbar = 2\pi\hbar$. The PA laser with optical frequency ν_l is detuned from the PA resonance by

$$\Delta \equiv \nu_l - [\nu(^1S_0 - ^3P_1) + \nu_n + \Delta\nu(I)], \quad (20)$$

where $\nu(^1S_0 - ^3P_1)$ is the atomic transition frequency, and $\hbar\nu_n$ is the energy of state n with respect to the free threshold. The detuning term $\Delta\nu(I)$ accounts for the ac Stark shift of the molecular resonance with respect to I .

The integral in Eq. 19 was approximated as a 53-term sum using Gauss-Laguerre quadrature. The quantities ($\ell_{\text{opt}}\gamma_m$), T , u_0 , and a term added to the detuning to represent the line center were allowed to vary. The parameter T is used as a check against the experimentally measured temperatures and agrees well with the experiment. The Stark shift term $\nu_s e^{-u/u_0}$ was included to account for the broadening of the atomic loss profile to the blue side of a molecular resonance due to the ac Stark shift induced by the trap. The molecular line width γ was extracted from the Monte-Carlo simulation in the next Section.

Monte-Carlo Simulation ($2k\ell_{\text{opt}}\gamma_m/\gamma \sim 1$)

To model the thermodynamic effects caused by the interplay of elastic and inelastic collisions in an anharmonic trap with evaporation, we use a Monte-Carlo simulation since analytic expressions such as those presented in the previous Section are not available. The simulation is based on classical particles moving in a conservative model potential that includes the Gaussian beam shapes as well as gravity. A commonly used method [13–15] to include collisions in such simulations is due to Bird [16] and detailed discussions of the method in the context of ultracold atoms in optical traps can be found in Refs. [17, 18]. The simulation procedure here is described in more detail in Ref. [8].

The simulation uses the elastic and inelastic cross section formulas derived in Section “Scattering Matrix, Cross Sections, and Collision Rates”:

$$\sigma_{\text{in}}(k) = \frac{4\pi}{k} \frac{\frac{\ell_{\text{opt}}\gamma_m}{\gamma}}{(\Delta + E/\hbar)^2/\gamma^2 + (1 + 2k\frac{\ell_{\text{opt}}\gamma_m}{\gamma})^2/4}, \quad (21)$$

$$\sigma_{\text{el}}(k) \simeq 2k \frac{\ell_{\text{opt}}\gamma_m}{\gamma} \sigma_{\text{in}}(k),$$

where the second relation is an approximation valid in an ideal ultracold gas like ^{88}Sr where the background scattering length a_{bg} can be neglected. For a gas at non-zero temperature, the detuning Δ includes the atomic motion and the trap ac Stark shift as in the previous section.

The initial particle distribution is synthesized by dropping atoms into the model potential and letting them evolve for several hundred ms without collisions (using an embedded Runge-Kutta method). Each particle is initially generated from independent Gaussian distributions along the trap eigenaxes, both in position and velocity. The initial widths of these Gaussian distributions are adjusted until the particle distribution after having settled in the model potential matches the experimental in-situ and TOF data when the PA laser is far detuned from the OFR resonance.

To calibrate the Monte-Carlo simulation, we modelled a three-dimensional isotropic harmonic trap of mK trap depth and checked the thermodynamic effects of inelastic and elastic collisions independently. Using a Gaussian initial phase-space density at several μK and only allowing inelastic collisions at a velocity-independent cross section, we recovered heating rates per particle that match the corresponding analytic expressions [8]. Similarly, we check cross-dimensional thermalization rates at a velocity-independent elastic cross section. We found that the average number of elastic collisions required for cross-dimensional thermalization in our simulation agrees [8] with the analytic expressions from Ref. [15].

The Monte-Carlo simulation also includes the effect of scattering from the atomic line. For the largest optical lengths in Fig. 4 of the main paper, the atomic scattering rate is $\sim 6 \text{ s}^{-1}$ corresponding to 1.2 photons scattered per atom during the 200 ms exposure time. At these scattering rates, the photon absorption along the PA laser direction and the random reemission change the resulting cloud widths by less than 10%. Due to the spontaneous reemission as a spherical wave, the mean free path of a scattered photon in a sample of $\text{OD} \sim 2$ is still larger than the typical cloud radii and we estimate that radiation trapping should only introduce a small correction.

The final particle distribution is then imaged by randomly scattering photons off of each particle and forming a histogram from the positions of the scattering events over the image pulse time of 50 μs , either in the trap or after TOF expansion for 1.5 ms. Random rescattering and corresponding velocity and position evolution are included, and the position histogram is blurred to account for the 4 μm image resolution. The final image is then analyzed in the same way as the experimental data to extract in-trap widths and TOF temperatures. By adding the final measurement step instead of calculating the covariance matrices of the position and velocity distributions directly, the quantitative agreement with the experiment was improved significantly in the regime of large inelastic losses.

Maximal scattering length modification

In the following, we build on the understanding from our current experiment and try to estimate the maximum scattering length under the most ideal conditions. We assume that atomic scattering is the dominant loss mechanism, that $k \rightarrow 0$, and that there is no extra molecular loss, such that $\gamma = 2\gamma_a$. There is also no spatial inhomogeneity, and thus it does not reflect the current experimental conditions. Theoretical calculations of the molecular line strength factors are used to make these estimates. Also note that the line strength factors are only order-of-magnitude estimates beyond $n < -5$.

The Optically-Modified Scattering Length Constrained by Atomic Light Scatter

In the $k \rightarrow 0$ limit, the scattering length change Δa due to an optical Feshbach resonance is given by

$$\Delta a = \ell_{\text{opt}} \frac{(\delta - \delta_0)\gamma_m}{(\delta - \delta_0)^2 + \gamma_m^2/4} = 2\ell_{\text{opt}} \frac{(\delta - \delta_0)\gamma_a}{(\delta - \delta_0)^2 + \gamma_a^2}, \quad (22)$$

where δ is 2π times the detuning from atomic resonance, δ_0 is the difference between the molecular and atomic resonance frequencies, γ_m is the molecular linewidth, γ_a is the atomic linewidth, and $\gamma_m = 2\gamma_a$. The quantity $\ell_{\text{opt}} = \xi I$, where I is the PA laser intensity and $\xi \equiv \frac{\lambda_a^3}{16\pi c} \frac{|\langle n|E \rangle|^2}{k}$ is a resonance-specific constant that describes the Sr+Sr molecular structure.

When using an OFR, δ must be chosen such that inelastic collisional loss is small. In this regime, loss due to atomic light scattering dominates. The atomic scattering rate Γ_{sc} is given by

$$\Gamma_{\text{sc}} = \frac{\gamma_a}{2} \frac{s_0}{1 + s_0 + 4(\delta/\gamma_a)^2}. \quad (23)$$

Here $s_0 = I/I_{\text{sat}}$, where I_{sat} is the saturation intensity of the atomic transition. Typically the experiment determines the maximum allowable value of Γ_{sc} , thereby constraining I . Under this constraint, I can be expressed as

$$I = I_{\text{sat}} \frac{2\Gamma_{\text{sc}}/\gamma_a}{1 - 2\Gamma_{\text{sc}}/\gamma_a} \left(1 + 4\frac{\delta^2}{\gamma_a^2}\right) \approx 8I_{\text{sat}} \left(\frac{\Gamma_{\text{sc}}}{\gamma_a}\right) \left(\frac{\delta}{\gamma_a}\right)^2, \quad (24)$$

where it has been assumed that $\gamma_a \gg \Gamma_{\text{sc}}$ and $\delta \gg \gamma_a$, the latter of which is true due to strontium's narrow intercombination line that is used in our work. The maximum ℓ_{opt} for a given detuning is simply

$$\ell_{\text{opt}} = \xi I = 8\xi I_{\text{sat}} \left(\frac{\Gamma_{\text{sc}}}{\gamma_a}\right) \left(\frac{\delta}{\gamma_a}\right)^2. \quad (25)$$

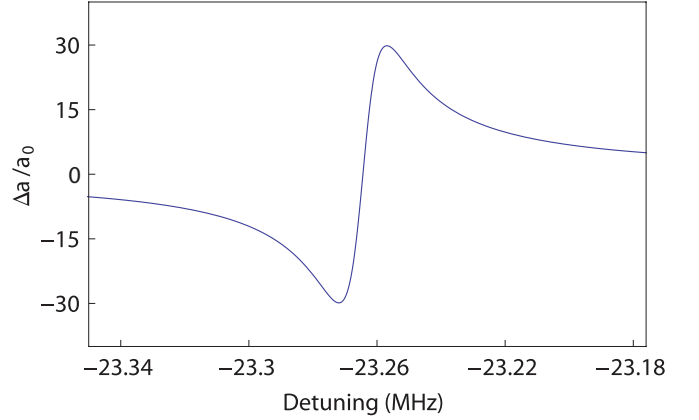


FIG. 6: Equation 26 plotted near molecular resonance. Here an ξ corresponding to the -23.264 MHz line has been used, $\Gamma_{\text{sc}} = 1 \text{ s}^{-1}$, $\gamma_a = 2\pi \times 7.5 \text{ kHz}$, and $I_{\text{sat}} = 3 \mu\text{W}/\text{cm}^2$. This behavior is well approximated by Δa_{dis} of Eq. 27.

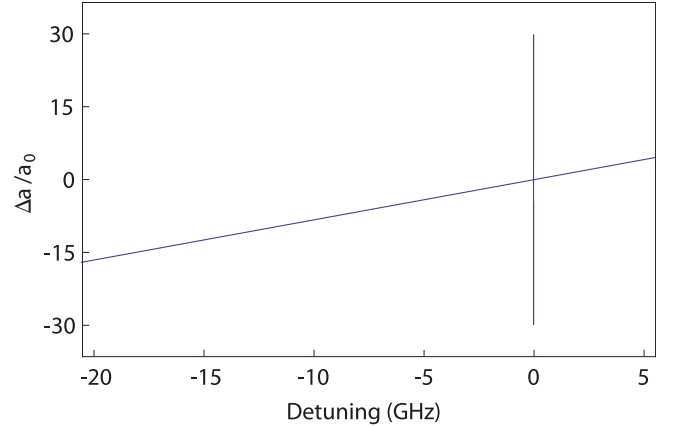


FIG. 7: Equation 26 plotted for large detunings. This plot was generated with the same values for ξ , δ_0 , Γ_{sc} , γ_a , and I_{sat} as those used in Fig. 6. This behavior of Δa for large detunings is well approximated by Δa_{lin} of Eq. 28. As will be discussed in Section “The Large Detuning Case,” these detunings are unphysical given the molecular structure and the coupled-channels theory discussed in the main text.

Thus Δa , constrained to a certain Γ_{sc} , is

$$\Delta a = 16\xi I_{\text{sat}} \left(\frac{\Gamma_{\text{sc}}}{\gamma_a}\right) \frac{\delta^2}{\gamma_a^2} \frac{(\delta - \delta_0)\gamma_a}{(\delta - \delta_0)^2 + \gamma_a^2}. \quad (26)$$

This expression is plotted in Figs. 6 and 7. Within tens of linewidths γ_m of $\delta = \delta_0$, the factor δ^2 in the numerator of Eq. 26 is slowly varying and can be approximated as δ_0^2 . Let Δa_{dis} refer to Δa in this regime. Therefore,

$$\Delta a_{\text{dis}} = 16\xi I_{\text{sat}} \left(\frac{\Gamma_{\text{sc}}}{\gamma_a}\right) \frac{\delta_0^2}{\gamma_a^2} \frac{(\delta - \delta_0)\gamma_a}{(\delta - \delta_0)^2 + \gamma_a^2}, \quad (27)$$

which has the dispersion shape of Fig. 6. When $\delta \gg \delta_0$, $|\Delta a|$ varies linearly with δ . Let Δa_{lin} be the expression

for Δa when $\delta \gg \delta_0$.

$$\Delta a_{\text{lin}} = 16\xi I_{\text{sat}} \left(\frac{\Gamma_{\text{sc}}}{\gamma_a} \right) \left(\frac{\delta}{\gamma_a} \right), \quad (28)$$

which describes the linear behavior evident in Fig. 7.

The Maximum Useful Scattering Length Near a Molecular Resonance

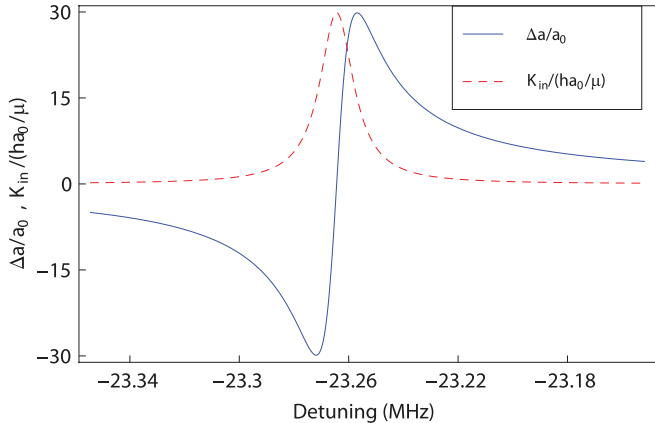


FIG. 8: Equation 26 plotted in blue and Eq. 29 plotted in red. This plot was generated with the same values for ξ , δ_0 , Γ_{sc} , γ_a , and I_{sat} as those used in Fig. 6. Note that K_{in} is significant near a molecular resonance but that this quantity drops off faster than Δa .

Near a molecular resonance where $|\Delta a|$ has dispersive behavior, it follows from Eq. 27 that $|\Delta a|$ has a local maximum at $|\delta - \delta_0| \approx \pm \gamma_a$. However, at these small detunings inelastic collisional loss must be considered. For $k \rightarrow 0$, the inelastic rate coefficient K_{in} is given by

$$K_{\text{in}} = \frac{4\pi\hbar\ell_{\text{opt}}}{\mu} \frac{\gamma_m^2}{(\delta - \delta_0)^2 + \gamma_m^2/4} \quad (29)$$

$$= \frac{16\pi\hbar\ell_{\text{opt}}}{\mu} \frac{\gamma_a^2}{(\delta - \delta_0)^2 + \gamma_a^2}.$$

Putting Eq. 25 into Eq. 29, it can easily be shown that the maximum value of K_{in} , denoted by $K_{\text{in}}^{\text{max}}$, occurs at $\delta \approx \delta_0$, consistent with the case when ℓ_{opt} in Eq. 22 is not constrained by atomic light scatter.

As Fig. 8 shows, inelastic loss (described by K_{in}) is significant near δ_0 . Nevertheless, this figure makes it apparent that one can choose a detuning that is just outside of the influence of K_{in} but that still yields a significant Δa . This detuning is implied upon setting $K_{\text{in}} = \kappa K_{\text{in}}^{\text{max}}$, where κ describes the fraction of molecular loss deemed acceptable by the experiment. Solving this equation for detuning yields that $\delta - \delta_0 \approx \pm \gamma_a / \sqrt{\kappa}$. Evaluating Eq. 26 at this detuning produces Δa_{max} ,

$$\Delta a_{\text{max}} \approx \pm 16\xi I_{\text{sat}} \sqrt{\kappa} \left(\frac{\Gamma_{\text{sc}}}{\gamma_a} \right) \left(\frac{\delta_0}{\gamma_a} \right)^2, \quad (30)$$

n	δ_0 (GHz)	δ_{lin} (GHz)
-2	-0.023	-7.22
-3	-0.221	-655
-4	-1.084	-1.57×10^4
-5	-3.460	-1.60×10^5
-6	-8.400	-9.40×10^5
-7	-17.0	-3.84×10^6

TABLE I: Theoretical values for δ_0 for the $n = -2$ through -7 0_u resonances and the associated values for δ_{lin} . Here $\kappa = 0.01$.

where Δa_{max} is the maximum scattering length change when Δa is dispersive and inelastic loss and atomic light scatter are negligible. The intensity corresponding to Δa_{max} , given by Eq. 24, is

$$I_{\Delta a_{\text{max}}} \approx 8I_{\text{sat}} \left(\frac{\Gamma_{\text{sc}}}{\gamma_a} \right) \left(\frac{\delta_0}{\gamma_a} \right)^2. \quad (31)$$

The Large-Detuning Case

Although $|\Delta a|$ in Eq. 26 seems to increase without bound when $\delta \gg \delta_0$, coupled-channels OFR theory (which so far has not been considered in this discussion) dictates that if $|\Delta a|$ is based on the n th resonance, the modification to the scattering length will vanish at some point before δ is equal to the detuning of the $(n-1)$ th resonance. See the main text for a further discussion of this coupled-channels effect. One must consider whether the molecular detuning $\delta - \delta_0$ can be sufficiently large to take advantage of the linear increase with δ but not so far that coupled-channels effects become a concern.

Let δ_{lin} be the detuning at which the magnitude of Δa_{lin} is equal to $|\Delta a_{\text{max}}|$. It follows that $|\delta_{\text{lin}}| = \sqrt{\kappa} \delta_0^2 / \gamma_a$. If δ_{lin} is comfortably outside the regime where coupled-channels effects are a concern, then the maximum useful scattering length occurs when one is many linewidths γ_m detuned from δ_0 but not far enough detuned to be close to other resonances. However, theoretical values for δ_0 make it clear that detuning to δ_{lin} would always require crossing another molecular resonance, so coupled-channels effects dictate that the maximum scattering length one can achieve is given by Δa_{max} (Eq. 30), occurring when δ is as close as possible to a molecular line, while molecular losses are constrained to a given level. Table I considers 6 different molecular resonances and their associated values of δ_{lin} , which are many orders of magnitude larger than δ_0 for subsequent resonances.

n	δ_0 (GHz)	ξ ($a_0/(W/cm^2)$)	$ \Delta a_{\max} $ (a_0)	$I_{\Delta a_{\max}}$ (W/cm 2)
-2	-0.023	6110	5.97	4.89×10^{-3}
-3	-0.221	32.8	2.92	0.443
-4	-1.084	27.9	59.3	10.6
-5	-3.460	3.30	71.5	108
-6	-8.400	0.272	34.7	637
-7	-17.0	0.012	6.21	2.61×10^3

TABLE II: Theoretical values for δ_0 and ξ for the $n = -2$ through -7 0_u resonances are used to calculate the maximum useful scattering length. The intensities required for these scattering lengths are also included. The optimal detuning for each resonance is given by $|\delta - \delta_0| = \gamma_a/\sqrt{\kappa} = 10\gamma$ for the value $\kappa = 0.01$ that was used in the table.

Conclusion

In light of Section “The Large-Detuning Case”, we conclude that for a given molecular line, the best optically-modified scattering length occurs for a laser detuned just outside the influence of inelastic loss and with an intensity just low enough to prevent heating due to atomic light scatter. This optimal detuning is given by $\delta - \delta_0 = \gamma_a/\sqrt{\kappa}$. Table II lists theoretical 0_u values for ξ and δ_0 as well the associated values for Δa_{\max} and $I_{\Delta a_{\max}}$. Values of $\Gamma_{sc} = 1$ s $^{-1}$ and $\kappa = 0.01$ have been used. For the strontium 1S_0 - 3P_1 line, $\gamma_a = 2\pi \times 7.5$ kHz and $I_{\text{sat}} = 3$ $\mu\text{W}/\text{cm}^2$. These numbers yield an optimal detuning of $\delta - \delta_0 = 2\pi \times 75$ kHz. The intensity column was included to point out that many resonances cannot be used on technical grounds (for instance intensities greater than a few kW/cm 2 are impractical for external cavity diode lasers).

Under the ideal conditions of zero temperature, no spatial inhomogeneity, no extra molecular loss and the assumption that atomic light scattering is the dominant loss mechanism, Table II shows that the resonance location of the $n = -5$ line is the best compromise between a large detuning from atomic resonance (which allows for more PA laser intensity without atomic light scatter) and the fact that ξ rapidly decreases with increasing $|\delta|$. According to Eq. 30, only moderate gains in Δa_{\max} can be achieved by allowing for more inelastic loss (when detuning closer to a molecular line) since any increase in K_{in} will only be accompanied by a $\sqrt{K_{\text{in}}}$ increase in $|\Delta a_{\max}|$.

More significant gains can be achieved by shortening experimental time scales to allow for larger values of Γ_{sc} since $|\Delta a_{\max}|$ is linear in Γ_{sc} .

-
- * Permanent address: The Niels Bohr Institute, Universitetsparken 5, 2100 Copenhagen, Denmark.
- [1] J. M. Hutson, New J. Phys. **9**, 152 (2007).
 - [2] C. Chin, R. Grimm, P. S. Julienne, and E. Tiesinga, Rev. Mod. Phys. **82**, 1225 (2010).
 - [3] J. P. Burke, Jr., Ph.D. thesis, Department of Physics, University of Colorado (1999), URL <http://jila.colorado.edu/thesis>.
 - [4] J. Bohn and P. Julienne, Physical Review A **60**, 414 (1999).
 - [5] R. Ciurylo, E. Tiesinga, and P. S. Julienne, Phys. Rev. A **74**, 022710 (2006).
 - [6] P. S. Julienne and F. H. Mies, Physical Review A **34**, 3792 (1986).
 - [7] R. Ciurylo, E. Tiesinga, and P. S. Julienne, Phys. Rev. A **71**, 030701 (2005).
 - [8] S. Blatt, Ph.D. thesis, Department of Physics, University of Colorado (2011), URL <http://jila.colorado.edu/yelabs/pubs/theses.html>.
 - [9] R. Grimm, M. Weidemüller, and Y. B. Ovchinnikov, arXiv:physics/9902072v1 (1999).
 - [10] M. M. Boyd, Ph.D. thesis, Department of Physics, University of Colorado (2007), URL <http://jila.colorado.edu/thesis/>.
 - [11] L. Allen and J. H. Eberly, *Optical Resonance and Two-Level Atoms* (Dover, 1987).
 - [12] T. Zelevinsky, M. M. Boyd, A. D. Ludlow, T. Ido, J. Ye, R. Ciurylo, P. Naidon, and P. S. Julienne, Phys. Rev. Lett. **96**, 203201 (2006).
 - [13] H. Wu and C. J. Foot, Journal of Physics B: Atomic, Molecular and Optical Physics **29**, L321 (1996).
 - [14] H. Wu, E. Arimondo, and C. Foot, Physical Review A **56**, 560 (1997).
 - [15] J. Goldwin, S. Inouye, M. Olsen, and D. Jin, Physical Review A **71**, 043408 (2005).
 - [16] G. A. Bird, *Molecular gas dynamics and the direct simulation of gas flows* (Clarendon Press, Oxford, 1994).
 - [17] M. E. Gehm, Ph.D. thesis, Department of Physics, Duke University (2003), URL <http://www.phy.duke.edu/research/photon/qoptics/theses/>.
 - [18] J. M. Goldwin, Ph.D. thesis, Department of Physics, University of Colorado (2005), URL <http://jila.colorado.edu/thesis/>.